Structural, electronic, and thermodynamic properties of curium dioxide: Density functional theory calculations

Ling Hou, Wei-Dong Li, Fangwei Wang, Olle Eriksson, and Bao-Tian Wang

Phys. Rev. B **96**, 235137 — Published 22 December 2017

DOI: 10.1103/PhysRevB.96.235137

Structural, electronic, and thermodynamic properties of curium dioxide: Density functional theory calculations

Ling Hou,[1,2,3] Wei-Dong Li,[1] Fangwei Wang,[3,4] Olle Eriksson,[5] and Bao-Tian Wang[2,3,*]

[1]*Institute of Theoretical Physics and Department of Physics, Shanxi University, Taiyuan 030006, China*
[2]*Institute of High Energy Physics, Chinese Academy of Sciences (CAS), Beijing 100049, China*
[3]*Dongguan Neutron Science Center, Dongguan 523803, China*
[4]*Beijing National Laboratory for Condensed Matter Physics, Institute of Physics, Chinese Academy of Sciences, Beijing 100080, China*
[5]*Department of Physics and Astronomy, Division of Materials Theory, Uppsala University, Box 516, SE-75120 Uppsala, Sweden*

We present a systematic investigation of the structural, magnetic, electronic, mechanical, and thermodynamic properties of CmO_2 with the local density approximation (LDA)+U and the generalized gradient approximation (GGA)+U approaches. The strong Coulomb repulsion and the spin-orbit coupling (SOC) effects on the lattice structures, electronic density of states, and band gaps are carefully studied, in comparing with other AO_2 (A=U, Np, Pu, and Am). Ferromagnetic configuration with half-metallic character is predicted to be energetically stable while a charge-transfer semiconductor is predicted for antiferromagnetic configuration. The elastic constants and phonon spectra show that the fluorite structure is mechanical and dynamical stable. Based on first-principles phonon density of state, the lattice vibrational energy is calculated using the quasi-harmonic approximation. Then, the Gibbs free energy, thermal expansion coefficient, specific heat, and entropy are obtained and compared with experimental data. The mode Grüneisen parameters are presented to analyze the anharmonic properties. The Slack relation is applied to obtain the lattice thermal conductivity in temperature range of 300-1600 K. The phonon group velocities are also calculated to investigate the heat transfer. For all these properties, if available, we compare the results of CmO_2 with other AO_2.

PACS numbers: 71.27.+a, 61.50.Ks, 62.20.-x, 63.20.dk

I. INTRODUCTION

Actinides and their compounds play an important role in the nuclear fuel cycle and exhibit many interesting physical characters due to their half-filled $5f$ orbital [1–5]. In any methodological framework, $5f$ actinide compounds are extremely challenging due to the interplay of various energy scales determined by electronic correlations on the f states, spin-orbit coupling (SOC), and crystal field effects and have attracted many attentions [4–15]. Without including the on-site Coulomb repulsion, the pure density functional theory (DFT) method would result in an error conducting ground state for many actinide dioxides [4–6, 8, 16, 17]. The insulator nature for these correlated electronic systems can be well reproduced using the DFT+U [17, 18], the hybrid density functional HSE (Heyd, Scuseria, and Enzerhof) [4, 5, 8], the self-interaction corrected local spin-density (SIC-LSD) approximation [6], and local density approximation (LDA) plus dynamical mean-field theory [7] calculations. The DFT+U calculations also reported better results of phonon spectra and phonon density of states (PhDOS) than the pure DFT for PuO_2 [19] and UO_2 [20], as examined by recent experiments [9, 12, 21]. The effects of SOC and crystal field are found critical important in obtaining the ground-state magnetic structures for some actinides [22–24]. In our previous study of PuH_2 and PuH_3 [22], we found that the reasonable phonon spectra can only be obtained by considering both the Coulomb repulsion and SOC simultaneously. The richness of these $5f$-multiorbital electronic properties in actinides supplies a treasure trove to investigate.

Among actinide oxides, the dioxides are the most stable and the most relevant members in nuclear fuel cycle [6]. Among the actinide dioxide series from Th (f^0) to Fm (f^{10}), PuO_2 and AmO_2 site at the intermediate zone and their $5f$ orbital has the largest overlap with oxygen-$2p$ orbital, before PuO_2 (ThO_2-NpO_2) the $5f$ orbital appears as localized behavior above the O-$2p$ orbital, while after AmO_2 (CmO_2-FmO_2) the $5f$ orbital appears as localized state below the O-$2p$ orbital.

In our previous studies, we have systematically investigated the ground-state properties (and high-pressure features) of ThO_2 [25], NpO_2 [17], PuO_2 [19], AmO_2 [26], and UO_2 [20]. While NpO_2 and UO_2 are predicted to be Mott insulators, PuO_2 and AmO_2 are found to be charge-transfer insulators. Along with increasing Z, the ionicity decreases from ThO_2 to AmO_2 [19, 26]. In the present work, we would like to extend our investigation to CmO_2 which has little been studied in experiments [27–30] and in theoretical calculations [5, 6, 31–37]. We will utilize the LDA+U and the generalized gradient approximation (GGA)+U schemes due to Dudarev *et al.* [18] to calculate the lattice parameters, magnetic states, electronic structure, mechanical features, phonon disper-

*Author to whom correspondence should be addressed. E-mail: wangbt@ihep.ac.cn

sions, and thermodynamic properties of CmO_2. We will discuss how the choice of U as well as the relativistic effects in terms of the SOC affect those properties. The nature of the chemical bonding of Cm-O will be presented, both qualitatively and quantitatively. Various thermodynamic properties which are important for CmO_2 in the fuel cycle will be presented in wide temperature range.

The present paper is organized as follows. In the following section, we present our calculation methodology and the theoretical formalism. In Sec. III, we give the results of structure, magnetic states, electronic structure, elasticity, chemical-bonding characters, phonon dispersions, and various thermodynamic properties. In Sec. IV, we present a summarizing discussion of the results. Then, we summarize the main conclusions of this work in Sec. V.

II. COMPUTATIONAL METHODS

A. Computational details

The calculations are performed at the DFT level, employing the projector augmented wave method as implemented in the VASP package [38]. The LDA and the Perdew, Burke, and Ernzerhof (PBE) form of the GGA [39, 40] are chosen to describe the exchange-correlation energy. A cutoff energy of 950 eV is used for the set of plane waves. The k-point meshs in the full wedge of the Brillouin zone (BZ) are sampled by 8×8×8 Monkhorst-Pack [41] grids. The curium $6s^2 7s^2 6p^6 6d^2 5f^6$ and oxygen $2s^2 2p^4$ electrons are treated as valence electrons. The strong on-site Coulomb repulsion among the localized Cm $5f$ electrons is described by using the LDA/GGA+U formulated by Dudarev *et al.* [18, 42, 43], where the double counting correction has been included as in the fully localized limit [44]. In this scheme, the total LDA (GGA) energy functional is of the form

$$E_{\mathrm{LDA(GGA)}+U} = E_{\mathrm{LDA(GGA)}} + \frac{U-J}{2}\sum_{\sigma}[\mathrm{Tr}\rho^{\sigma} - \mathrm{Tr}(\rho^{\sigma}\rho^{\sigma})], \quad (1)$$

where ρ^{σ} is the density matrix of f states with spin σ, while U and J are the spherically averaged screened Coulomb energy and the exchange energy, respectively. In our study, the Coulomb U is treated as a variable, while the parameter J is fixed to be J=0.5 eV. Due to the fact that only the difference between U and J is significant in Dudarev's approach [18], for simplicity, we label them as one single parameter, named as U. In some cases of our calculations, the full relativistic effects are included in terms of the SOC. Comparing with the scheme through the solution of Dirac equation for SOC, the perturbative treatment of SOC implemented in VASP is also a good approximation for actinides [20, 45]. The theoretical equilibrium volume V, bulk modulus B, and pressure derivative of the bulk modulus B' are obtained by fitting the energy-volume data in the third-order Birch-Murnaghan equation of state (EOS) [46].

B. Elastic properties and Debye temperature

Based on the Hooke's law, the elastic constants C_{11}, C_{12}, and C_{44} are calculated by applying stress tensors with various small strains onto the equilibrium structures. The strain amplitude δ is varied in steps of 0.006 from δ=-0.036 to 0.036. A detailed calculation method can be found in Refs. [19, 47]. After having obtained the elastic constants, the polycrystalline bulk modulus B and shear modulus G are calculated from the Voigt-Reuss-Hill (VRH) approximations [48] through $B = \frac{1}{2}(B_V + B_R)$ and $G = \frac{1}{2}(G_V + G_R)$. The Young's modulus E and Poisson's ratio ν are calculated through $E = 9BG/(3B+G)$, and $\nu = (3B-2G)/[2(3B+G)]$. The Debye temperature θ_D can be determined from the elastic constants within the Debye theory, in which the vibrations of the solid are considered as elastic waves, and the Debye temperature of the solid is related to an averaged sound velocity [49], which is calculated by

$$\theta_D = \frac{h}{k_B}\left(\frac{3n}{4\pi\Omega}\right)^{1/3} \upsilon_m, \quad (2)$$

where h and k_B are Planck and Boltzmann constants, respectively, n is the number of atoms in the molecule, Ω is molecular volume, and υ_m is the average sound wave velocity. Approximately, υ_m can be given by

$$\upsilon_m = \left[\frac{1}{3}\left(\frac{2}{\upsilon_t^3} + \frac{1}{\upsilon_l^3}\right)\right]^{-1/3}, \quad (3)$$

where $\upsilon_t = \sqrt{G/\rho}$ (ρ is the density) is the transverse elastic wave velocity and $\upsilon_l = \sqrt{(3B+4G)/3\rho}$ is the longitudinal elastic wave velocity.

C. Phonon dispersion and thermodynamic properties

We use the direct method as implemented in the YPHON code [50] to calculate the phonon curves in the BZ and the corresponding phonon density of states (PhDOS). In calculating the force constants, a 2×2×2 supercell of the primitive cell is sampled with a 6×6×6 k points.

Based on our calculated total energy and PhDOS, we can further calculate the thermodynamic properties using the quasiharmonic approximation (QHA) [20, 51]. Under the QHA, the Gibbs free energy $G(T,P)$ at temperature (T) and pressure (P) can be written as $G(T,P) = F(T,V) + PV$. The Helmholtz free energy $F(T,V)$ at T and volume (V) is defined as

$$F(T,V) = E(V) + F_{\mathrm{vib}}(T,V) + F_{el}(T,V), \quad (4)$$

where $E(V)$ is the ground-state total energy, $F_{\rm vib}(T,V)$ is the vibrational energy of the lattice ions and $F_{el}(T,V)$ is the thermal electronic contribution. $F_{\rm vib}(T,V)$ can be calculated by

$$F_{\rm vib}(T,V) = k_B T \int_0^\infty g(\omega) \ln\left[2\sinh\left(\frac{\hbar\omega}{2k_BT}\right)\right] d\omega, \tag{5}$$

where ω represents the phonon frequencies and $g(\omega)$ is the PhDOS. F_{el} can be calculated by [52, 53]

$$F_{el}(T,V) = E_{el} - TS_{el} = -\frac{(\pi k_B)^2}{6} D(\epsilon_F) T^2, \tag{6}$$

where E_{el} is the internal electronic energy [54] written as $E_{el} = \frac{(\pi k_B)^2}{6} D(\epsilon_F) T^2$, S_{el} is the electronic contribution to the entropy written as $S_{el} = \int_0^T \frac{1}{T'} \left(\frac{\partial E}{\partial T'}\right)_V dT' = 2\frac{E_{el}}{T}$, $D(\epsilon_F)$ is the electronic density of state at the Fermi level.

The specific heat at constant volume C_V can be calculated by [19]

$$C_V = k_B \int_0^\infty g(\omega) \left(\frac{\hbar\omega}{k_BT}\right)^2 \frac{\exp\frac{\hbar\omega}{k_BT}}{\left(\exp\frac{\hbar\omega}{k_BT} - 1\right)^2} d\omega, \tag{7}$$

while the specific heat at constant pressure C_P can be obtained through the thermodynamic relationship $C_P - C_V = \alpha_V^2(T) B(T) V(T) T$, where the thermal-expansion coefficient $\alpha_V(T)$ is written as $\alpha_V(T) = \frac{1}{V}(\frac{\partial V}{\partial T})_P$.

For the fluorite type curium dioxide, the efficient heat carriers were to be their acoustic branches [55]. For temperature $T \geqslant \theta_D$, we predict the lattice thermal conductivity k_L here by the Slack theory [56, 57]

$$k_L = A \frac{\bar{M}\theta_D^3(T)\delta(T) n^{1/3}}{\gamma^2(T) T}, \tag{8}$$

where A is a physical constant with the value of 3.1×10^{-6}, $\bar{M}$ is the average mass per atom in the crystal, θ_D is the Debye temperature, δ is the cube root of the average volume per atom, n is the number of atoms in the primitive unit cell, and $\gamma(T)$ is the Grüneisen parameter. The units of k_L and δ in Eq. (8) are $\mathrm{Wm^{-1}k^{-1}}$ and Å, respectively. With reasonable expressions for the Debye temperature and acoustic Grüneisen parameter to describe the harmonic phonon branches and the anharmonic interactions between different phonon branches, Eq. (8) can provide accurate predictions for a material's thermal conductivity.

Within the isotropic approximation, $\theta_D(T)$ can be calculated by [58]

$$\theta_D(T) = \frac{\hbar}{k_B} [6\pi^2 V^{1/2}(T) n]^{1/3} f(\nu) \sqrt{\frac{B(T)}{M}}, \tag{9}$$

where $B(T)$ is the bulk modulus, M is the molecular mass per formula unit, ν stands for the materual's Poisson ratio, and $f(\nu)$ can be expressed as

$$f(\nu) = 3^{1/3} \left[2\left(\frac{2}{3}\frac{1+\nu}{1-2\nu}\right)^{3/2} + \left(\frac{1}{3}\frac{1+\nu}{1-\nu}\right)^{3/2}\right]^{-1/3}. \tag{10}$$

The mode Grüneisen parameter $\gamma_j(\mathbf{q})$ describing the phonon frequency shift with respect to the volume can be expressed as

$$\gamma_j(\mathbf{q}) = -\frac{d[\ln\omega_j(\mathbf{q},V)]}{d[\ln V]}. \tag{11}$$

The acoustic Grüneisen parameter $\gamma(T)$ is defined as the weighted average of the mode Grüneisen parameter for all acoustic phonon branches, which can be calculated by

$$\gamma(T) = \frac{\alpha_V(T) B(T) V_m(T)}{C_V(T)}, \tag{12}$$

where $\alpha_V(T)$ is the thermal expansion coefficient, $V_m(T)$ is the volume per mole, $B(T)$ is the bulk modulus and $C_V(T)$ is the specific heat.

III. RESULTS

A. Structure and magnetic states

At room temperature and zero pressure conditions, CmO_2 crystallizes in a CaF_2-like ionic structure with space group $Fm\bar{3}m$ (No. 225) [28, 59], which is shown in Fig. 1. Its cubic unit cell is composed of four CmO_2 formula units (f.u.) with the curium atoms and the oxygen atoms in $4a$(0, 0, 0) and $8c$(0.25, 0.25, 0.25) Wyckoff sites, respectively. In experiment [27], a phase transition to an orthorhombic structure at pressure range of 30−40 GPa has been reported. In the present work, we only study the ground-state fluorite phase. Since the magnetic structure of CmO_2 is still unclear in experiments [30] and most actinide dioxides stable as (100) AFM state [19, 20, 60–62], we should consider the NM, FM, and (100) AFM configurations in our following study. For simplicity, we label (100) AFM as AFM.

As shown in Table I, the NM state of CmO_2 is not energetically favorable compared with the AFM and FM states. At the same time, the dependence of the total energy (per f.u. at respective optimum geometries) on U for both AFM and FM configurations are shown in Fig. 2. It is clear that the FM arrangement always has the lowest energy. Using a typical value of U=4 eV, the total-energy differences ($\Delta E = E_{\rm AFM} - E_{\rm FM}$) are calculated to be 82, 25, 151, 68, 132, and 35 meV with GGA, LDA, GGA+U, LDA+U, GGA+U+SOC, and LDA+U+SOC, respectively. The strong Coulomb repulsion and/or the SOC have not turned over the stability of the magnetic states.

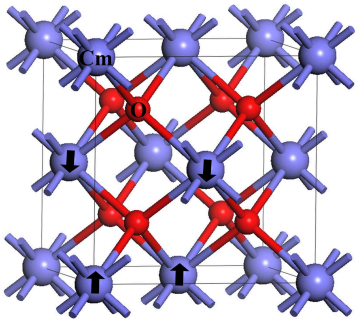

FIG. 1: (Color online) Unit cell of fluorite CmO_2. Large violet atoms are Cm while small red atoms are O. The black arrows illustrate the (100) AFM ordering.

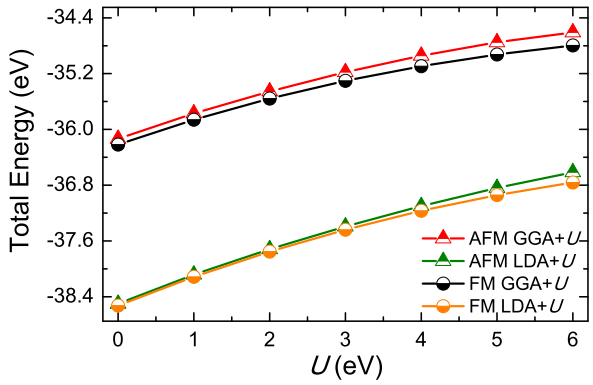

FIG. 2: (Color online) Dependences of the total energies (per f.u.) on U for FM and AFM states.

In Fig. 3, we compare our optimized a_0 and B with available experimental values [27, 29]. While LDA underestimates the value of a_0, the GGA overestimates it. After including the strong Coulomb repulsion, with LDA+U, the a_0 is steadily increased to close to the experimental value with a typical value of U=3 or 4 eV. Using U=4 eV, the LDA+U gives a_0=5.378 (5.341) Å for FM (AFM) state which is close to the experimental value of 5.359 Å [29] as well as the SIC-LSD value of 5.37 Å [6].

We show in Fig. 4(a) the lattice constants of AFM AO_2 (A=U, Np, Pu, Am, and Cm) series. Results calculated with LDA+U [17, 19, 20] and LDA+U+SOC [20] are slightly smaller than the corresponding experimental values [29] but the trends agree, i,e., the lattice constants decrease almost linearly with increasing Z. This indicates that our results are believable. Through comparing, we note that the differences raised by including the SOC are very limited. On the whole, the LDA+U(+SOC) results are consistent with the HSE lattice constants [5, 62], but smaller than the corresponding SIC-LSD lattice constants [6].

For bulk modulus B, as indicated in Fig. 3(b) and Ta-

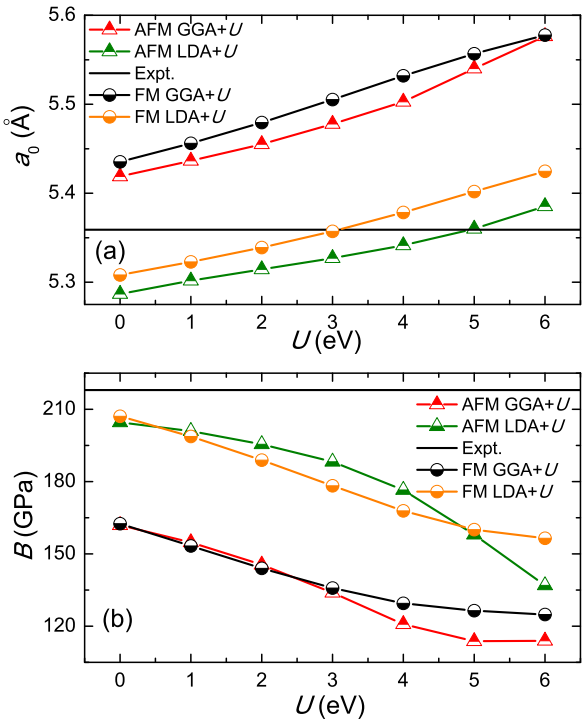

FIG. 3: (Color online) Dependences of the (a) lattice parameter and (b) bulk modulus on U for FM and AFM phases.

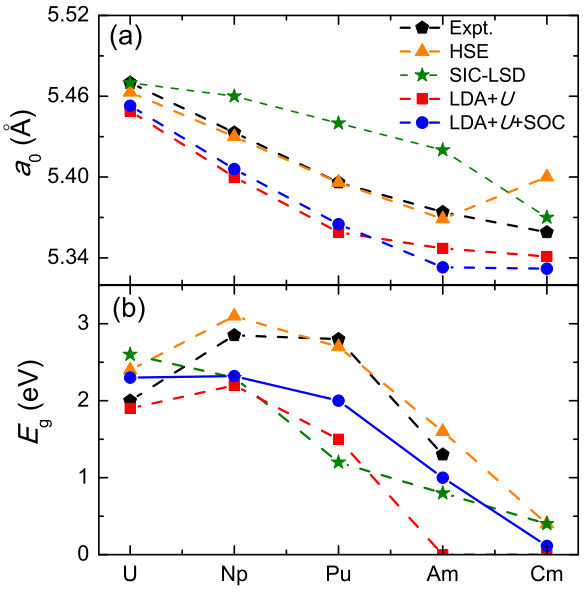

FIG. 4: (Color online) (a) Lattice parameters and (b) band gaps of the actinide dioxides in AFM state calculated with the LDA+U(+SOC) (U=4 eV) methods. Some values are from our previous calculations [17, 19, 20]. Experimental values from Refs. [29, 68–70], the SIC-LSD values from Ref. [6], and the HSE values from Refs. [5, 62] are also shown for comparison.

TABLE I: Equilibrium lattice constants (a_0), total energy (E), bulk modulus (B), pressure derivative of the bulk modulus (B′), and magnetic moments (μ_s and μ_l) for NM, FM and AFM states of CmO_2 calculated with GGA/LDA, GGA/LDA+U (U=4 eV), and GGA/LDA+U+SOC (U=4 eV) at 0 GPa. For comparison, experimental values and results from other calculations are also listed.

Mag.	Method	a_0 (Å)	E (eV)	B (GPa)	B'	$\mu_s(\mu_l)$ (μ_B)
NM	GGA	5.265	-32.582	198.6	4.4	
	GGA+U	5.381	-29.396	194.1	4.5	
	GGA+U+SOC	5.410	-37.538	193.3	4.4	
	LDA	5.149	-35.825	239.7	4.4	
	LDA+U	5.272	-32.304	230.3	4.4	
	LDA+U+SOC	5.303	-40.488	227.0	4.3	
FM	GGA	5.435	-36.217	162.5	4.9	6.13
	GGA+U	5.532	-35.093	129.5	4.5	6.60
	GGA+U+SOC	5.523	-39.390	129.6	4.7	6.41(-0.19)
	LDA	5.308	-38.526	207.1	4.8	5.91
	LDA+U	5.378	-37.168	167.9	4.8	6.37
	LDA+U+SOC	5.368	-41.600	170.2	4.8	5.94(-0.32)
AFM	GGA	5.419	-36.135	161.9	4.8	5.98
	GGA+U	5.503	-34.942	120.8	4.4	6.47
	GGA+U+SOC	5.490	-39.258	123.7	5.6	6.22(-0.33)
	LDA	5.287	-38.501	204.6	4.6	5.71
	LDA+U	5.341	-37.100	176.5	5.9	6.15
	LDA+U+SOC	5.332	-41.565	188.0	6.1	5.68(-0.52)
	Expt.	5.359[a]		218(5)[b]	7(1)[b]	
	FPLMTO[c]			218.0	3.1	
	SIC-LSD[d]	5.37		212		

[a]Reference [29], [b]Reference [27], [c]Reference [32], [d]Reference [6]

ble I, including of the strong Coulomb repulsion Hubbard U parameter in our calculations will lead to large offset with respect to the experimental values [27] and theoretical values [6, 32]. Here, one may doubt our results. However, concerning the old experimental values [27, 63] of B for AO_2, results of PuO_2 and AmO_2 were found by a new experiment [64] being largely overestimated. Besides, the high-pressure experiments [27] were performed at ambient temperature but our results are only valid at 0 K. A paramagnetic model [65] should be more reasonable to predict a smaller bulk modulus, however, this kind of calculation is outside of our present work. Anyway, our GGA+U calculations for NM, FM, and AFM sates give B=194.1, 129.5, 120.8 GPa, respectively, which are in good agreement with recent GGA+U calculations [37] (B=203.6, 134.7, 128.6 GPa, respectively). Thus, further experimental and theoretical studies are needed before any general conclusions can be drawn about our calculated values of B. From Fig. 3(b), one can find that the LDA+U results (156−207 GPa)/(137−204 GPa) of FM/AFM state are always higher than the GGA results

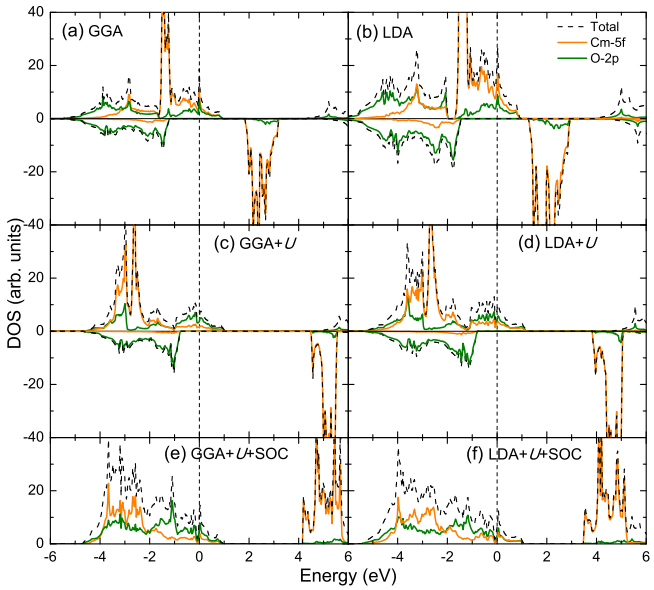

FIG. 5: (Color online) The total and the orbital-resolved local DOSs for FM state calculated with GGA/LDA, GGA/LDA+U, GGA/LDA+U+SOC using U=4 eV. The Fermi energy level is set at zero.

(125−162 GPa)/(114−162 GPa). This is understandable since the lattice constants are always overestimated using GGA. Using U=4 eV, we obtain B=167.9/176.5 GPa for FM/AFM state with LDA+U. After including SOC, these values are increased to 170.2 and 188.0 GPa, respectively, which are closer to the experimental value of 218 GPa [27].

Assuming a $5f^6$ dominated configuration for Cm in a +4 valence state, a single particle picture, according to the third Hund's rule, tells us the total momentum **J** would vanish. This picture is of course inappropriate due to various effects including crystal field splittings, covalency/hybridization effects, and the many-body nature of the local Cm moment. We can evaluate the spin and orbital contribution to the magnetic moment (μ_s and μ_l). In calculations, the direction of the magnetic moment is set along z-axis. Results obtained with GGA/LDA, GGA/LDA+U and GGA/LDA+U+SOC are tabulated in Table I. The values of μ_s with GGA/LDA+U are slightly larger than that with GGA/LDA and GGA/LDA+U+SOC. In particular, the LDA+U+SOC calculations give values of μ_s=5.68 μ_B and μ_l=-0.52 μ_B for AFM state, which result in a total magnetic moment μ_{total}=5.16 μ_B. These values are in good agreement with previous DFT value of μ=5.21 μ_B [6] with SIC-LSD, but larger than the experimental magnetic moment of μ_{eff}=3.36±0.06 μ_B [30]. The difference between calculations and experiment need further neutron diffraction experiments to clarify, if large enough sample can be obtained.

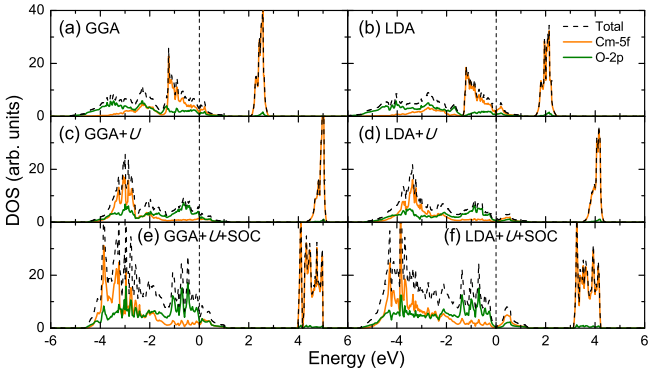

FIG. 6: (Color online) The total and the orbital-resolved local DOSs for AFM state calculated with GGA/LDA, GGA/LDA+U, GGA/LDA+U+SOC using U=4 eV. The Fermi energy level is set at zero.

B. Electronic structure

For half-filled $5f$ electronic systems, the strong Coulomb repulsion effect as well as the relativistic effect of SOC are both critical in obtaining reasonable electronic structures. This fact has been well established in many actinide dioxides and hydrides [5, 6, 17, 19, 20, 22, 26, 61, 66, 67]. For our present system CmO_2, although there are no experimental results to compare, the effects of strong Coulomb repulsion and SOC should be considered [5, 6].

From our calculated electronic density of states (DOS), Figs. 5 and 6, one can find that including of the strong Coulomb repulsion effect (using U=4 eV) pushes the $5f$ electrons occupation from near the Fermi energy level (-2 to 0 eV) to deeper energy level (-4 to -2 eV). The main occupation near the Fermi level is turned over from U-$5f$ to O-$2p$. The peak-type distribution of the $5f$ electrons is smoothed. This kind of electronic occupation is in good agreement with result with HSE [5]. For FM state, we only obtain half-metallic state even increasing U to 6 eV. As for AFM state, a metallic state is predicted with LDA+U while a charge-transfer semiconductor with indirect band gap of 113 meV is obtained with LDA+U+SOC. This value of the band gap is smaller than previous calculated values of 0.4 eV with HSE [5] and SIC-LSD [6] as well as 0.57 eV with GGA+U+SOC (U=4 eV) [37]. The origin of this discrepancy is unknown and need further experiments to clarify. We also perform calculations for NM state. Using GGA/LDA+U and GGA/LDA+U+SOC, we calculate the band gaps to be 1.90/1.80 and 1.94/2.02 eV, respectively, which are close to previous calculated values of ∼2 eV with LDA+U [35].

For band gaps of the AFM state in the AO_2 series, compared with LDA+U [17, 19, 20], using LDA+U+SOC [20] could result in better consistency with the experiments [68–70] [see Fig. 4(b)]. The trends, increase firstly from UO_2 to NpO_2 and then decrease from PuO_2 to CmO_2, agree fairly well with experiments. This indicates that our results are believable. The largest discrepancy between the LDA+U calculations and experiments occurs for PuO_2 and AmO_2, where the gaps differ by some 1.3 eV. A zero band gap is predicted with LDA+U for AmO_2 and CmO_2. On the whole, the LDA+U+SOC results are consistent with the SIC-LSD band gaps [6], but smaller than the corresponding HSE gaps [5, 62]. Therefore, the effects of the SOC on the electronic structures as well as the global minimum are crucial for AO_2 [20, 62, 71].

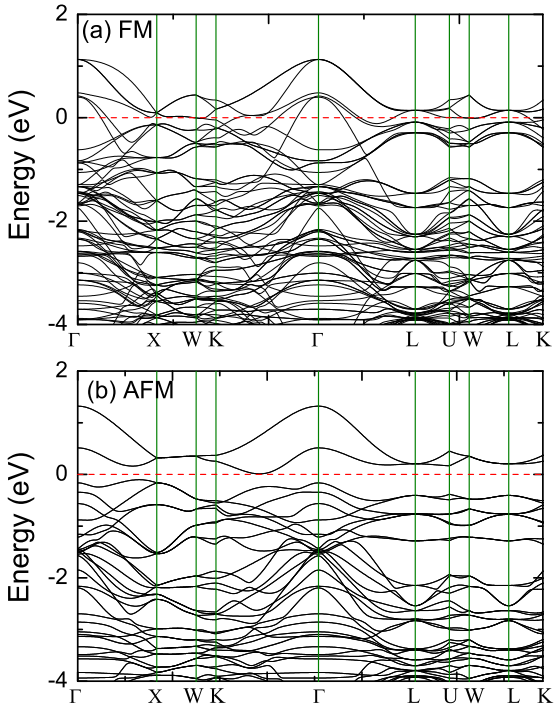

FIG. 7: (Color online) The band structures for FM and AFM states calculated with LDA+U+SOC using U=4 eV. The Fermi energy level is set at zero.

To clearly view the electronic structure, we plot in Fig. 7 the band structure of the FM and AFM states calculated with LDA+U+SOC. For metallic FM state, there are at least three bands that cross the Fermi level along the Γ-X, Γ-K, Γ-L, L-K, and W-K high-symmetry directions, which, results in a three-dimensional conductivity. For semiconducting AFM state, the conduction-band minimum locates along the Γ-K and the valence-band maximum sites along the Γ-X.

C. Elasticity and chemical bonding

As indicated in Refs. [20, 71] for typical actinide dioxides, the effects of the SOC on the elastic properties, phonon spectrum, and thermodynamic properties can be

TABLE II: Elastic constants (C_{11}, C_{12}, C_{44}), bulk modulus (B), shear modulus (G), Young's modulus (E), Poisson's ratio (ν), density (ρ), transverse (υ_t), longitudinal (υ_l), average (υ_m) sound velocity, and Debye temperature (θ_D) for FM and AFM states with GGA/LDA and GGA/LDA+U (U=4 eV).

Magnetism	Method	C_{11} (GPa)	C_{12} (GPa)	C_{44} (GPa)	B (GPa)	G (GPa)	E (GPa)	ν	ρ (g/cm^3)	υ_t (m/s)	υ_l (m/s)	υ_m (m/s)	θ_D (K)
FM	GGA	289.4	102.8	35.1	165.0	52.6	142.6	0.356	11.546	2134.4	4513.0	2401.6	301.4
	GGA+U	207.8	92.4	38.7	130.8	45.4	122.2	0.344	10.951	2037.4	4181.2	2289.0	282.2
	LDA	355.6	137.1	54.6	209.9	72.4	194.7	0.345	12.395	2416.2	4972.0	2715.0	348.8
	LDA+U	279.9	114.9	47.2	169.9	59.2	159.0	0.344	11.914	2228.2	4569.5	2503.2	317.4
AFM	GGA	298.0	97.8	19.1	164.5	39.9	110.7	0.388	11.650	2841.6	4323.0	3112.0	391.0
	GGA+U	199.6	84.5	14.0	122.9	25.8	72.2	0.402	11.125	1521.8	3759.3	1723.2	213.6
	LDA	367.2	127.4	43.7	207.3	66.4	180.0	0.355	12.545	2300.6	4856.0	2588.5	333.9
	LDA+U	312.8	113.4	36.0	179.9	54.9	149.4	0.362	12.165	2124.0	4561.0	2391.8	305.4

TABLE III: Elastic constants (C_{11}, C_{12}, C_{44}), bulk modulus (B), shear modulus (G), Young's modulus (E), Poisson's ratio (ν), density (ρ), transverse (υ_t), longitudinal (υ_l), average (υ_m) sound velocity, and Debye temperature (θ_D) for AFM state. For comparison, the theoretical results of other actinide dioxides(AmO_2, PuO_2, NpO_2, UO_2, ThO_2) with LDA+U (U=4 eV) are also listed.

	C_{11} (GPa)	C_{12} (GPa)	C_{44} (GPa)	B (GPa)	G (GPa)	E (GPa)	ν	ρ (g/cm^3)	υ_t (m/s)	υ_l (m/s)	υ_m (m/s)	θ_D (K)
ThO_2[a]	349.5	111.4	70.6	191	87.1	226.8	0.302	9.880	2969.1	5575.5	3317.3	402.6
UO_2[b]	389.3	138.9	71.3	222.4	89.5	236.7	0.323	11.084	2841.8	5552.7	3183.4	398.1
NpO_2[c]	399.5	145.5	72.9	230	91.2	241.7	0.325	11.351	2834.6	5565.6	3176.4	401.2
PuO_2[d]	319.6	177.8	74.5	225	73.0	197.7	0.354	11.896	2477.9	5205.8	2787.2	354.5
AmO_2	352.9	109.9	80.0	190.9	94.6	243.6	0.287	11.953	2813.7	5150.5	3137.8	400.2
CmO_2	312.8	113.4	36.0	179.9	54.9	149.4	0.362	12.165	2124.0	4561.0	2391.8	305.4

[a]Results of NM state with GGA method from Reference [25], [b]Reference [20], [c]Reference [17], [d]Reference [19]

neglected. Thus, in the following, we will present results obtained without SOC.

The elastic constant, various moduli, Poisson's ratio, density, elastic wave velocities, and Debye temperatures for FM and AFM states are presented in Table II. Obviously, both AFM and FM states of CmO_2 are mechanically stable because their elastic constants satisfy the mechanical stability criteria [72] of the cubic structure: $C_{11} > 0$, $C_{44} > 0$, $C_{11} > |C_{12}|$, $(C_{11}+2C_{12}) > 0$. The derived bulk moduli for FM/AFM calculated with GGA/LDA(+U) are close to that obtained by the EOS fitting. The discrepancies between these two methods are within 4 GPa. This means that our calculations are consistent and reliable. We note that our calculated C_{11}, C_{12}, C_{44} are smaller by 81.8, 15.9 and 12.8 GPa compared to a recent GGA+U study [37]. Their derived bulk modulus (B=160.730 GPa) from elastic constants is inconsistent with their EOS fitting result (B=128.62 GPa). So, our results are more reliable.

To understand the elastic properties of CmO_2 in AO_2 series, we compare in Table III the elastic constants, elastic moduli, elastic wave velocities, and Debye temperature of CmO_2 with corresponding results of other actinide dioxide [17, 19, 20, 25]. Results of NM ThO_2 [25] were calculated with GGA while results of UO_2 to CmO_2 in AFM state were/are obtained with LDA+U (U=4 eV) [17, 19, 20]. We only compare the results for AFM state (UO_2 to CmO_2) which is the most stable magnetic configuration for most AO_2. Among these AO_2 series, the values of the elastic constants and the elastic moduli for CmO_2 are the smallest. This is partially due to the number of the $5f$ electrons is increased from U to Cm. Another reason may find its answer from analyzing their electronic DOS. For middle AO_2, PuO_2 [19] and AmO_2 [26], the degeneracy of the $5f$-$2p$ orbitals in energy below the Fermi level is dominant. However, this kind of degeneracy is very weak for UO_2 [20], NpO_2 [17], and CmO_2. This kind of orbital mixing and covalency has also been noticed in previous HSE study [5].

The elastic properties of materials is tightly related to their chemical bonding. To study the chemical bonding for CmO_2, we plot the isosurfaces of the charge density and difference charge density in Fig. 8. While the two-dimensional isofurfaces are plotted in the $(1\bar{1}0)$ plane, the three-dimensional one are viewed along the [001] direction. The difference charge density is obtained by subtracting the densities of noninteracting component systems, ρ(Cm)+ρ(O), from the density of the CmO_2,

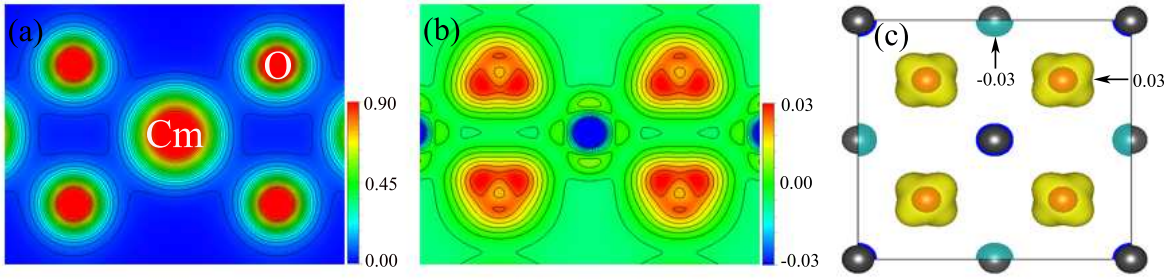

FIG. 8: (Color online) (a) Valence charge density and (b) difference charge density of FM state in the $(1\bar{1}0)$ plane calculated with LDA+U using U=4 eV. The contour lines for the valence charge density are drawn from 0.0 to 0.8 at 0.05 e/au^3 intervals while for the difference charge density are drawn from -0.03 to 0.03 at 0.005 e/au^3 intervals. In (c), we show a three-dimensional isosurface for the difference charge density.

TABLE IV: Calculated charge (Q_B) and volumes (V_B) according to Bader partitioning as well as the bond lengths and charge density values at bond points (CD_b) for FM and AFM states with GGA/LDA and GGA/LDA+U (U=4 eV) approaches.

Magnetism	Methods	Q_B(Cm) (e)	Q_B(O) (e)	V_B(Cm) (Å^3)	V_B(O) (Å^3)	Cm-Cm (Å)	Cm-O (Å)	O-O (Å)	CD_b(Cm-Cm) (e/au^3)	CD_b(Cm-O) (e/au^3)	CD_b(O-O) (e/au^3)
FM	GGA	15.74	7.13	15.40	12.37	3.843	2.354	2.718	0.022	0.072	0.0022
	GGA+U	15.79	7.10	16.10	13.11	3.912	2.395	2.766	0.020	0.064	0.0019
	LDA	15.78	7.11	14.72	11.33	3.753	2.298	2.654	0.026	0.081	0.0028
	LDA+U	15.80	7.10	15.16	11.87	3.803	2.329	2.689	0.024	0.075	0.0025
AFM	GGA	15.74	7.13	15.41	12.18	3.832	2.346	2.709	0.022	0.073	0.0023
	GGA+U	15.75	7.13	15.92	12.87	3.891	2.383	2.751	0.021	0.066	0.0020
	LDA	15.80	7.10	14.70	11.12	3.738	2.289	2.643	0.026	0.083	0.0029
	LDA+U	15.74	7.13	14.92	11.59	3.777	2.313	2.671	0.025	0.078	0.0026

while maintaining the positions of the component systems at the same location as in CmO_2. These pictures are obtained for FM state with LDA+U (U=4 eV). As indicated in Fig. 8(a), the charge densities around the Cm and O ions have almost a spherical distribution with slightly deformed distribution towards their nearest neighboring atoms to form the Cm-O bonding. It is the network of these Cm-O bonds that responsible for the stability. We will carefully investigate the ionic/covalent natures of the Cm-O bonds in the following. The charge density around Cm and O ions is high while there are almost no remaining charges in the large octahedral-hole interstitial region. From the two-dimensional and three-dimensional isosurfaces of the difference charge density, presented in Figs. 8(b) and (c), respectively, we find that the main contribution to the charge accumulation is from O atoms, not Cm.

To study the covalent and ionic characters quantitatively, we calculate the line charge density along the Cm-Cm, Cm-O, and O-O bonds and also perform the Bader analysis. The Bader charges, Bader volumes, bond lengths, and line charge density at the corresponding bond points (CD_b) are listed in Table IV. From these results, we can deduce some points for CmO_2: i> The CmO_2 are bonded by Cm-O bonds with mixed feature of covalent and ionic. The CD_b value for Cm-O of 0.064-0.081 e/au^3 for FM state and 0.066-0.083 e/au^3 for AFM state are lower than 0.104 e/au^3 found for the Si covalent bond [73], but prominently higher than 0.007 e/au^3 found for the Na-Cl bond in the typical ionic crystal NaCl [73]. Besides, from our calculated Bader charges, we find that each Cm atom loses 2.20-2.26 (2.20-2.26) electrons to O atoms for FM (AFM) state. The ionic charge for FM and AFM states of CmO_2 can be represented as $Cm^{2.20+}O^{1.10-}$ and $Cm^{2.26+}O^{1.13-}$, respectively; ii> The differences between AFM and FM are very small; iii> The effects brought by the strong Coulomb repulsion are also limited. After including Hubbard U, the bond lengths are increased and the CD_b are decreased. In addition, the covalent property as presented by the value of the CD_b (around 0.53 e/Å^3 for AFM state with LDA+U) for CmO_2 is comparable to that for UO_2, NpO_2, and PuO_2 [19]. The ionicity of AO_2 is again found to show decreasing trend with increasing Z [19].

D. Phonon dispersion

Employing the Hellmann-Feynman theorem and the direct method, we have calculated the phonon curves

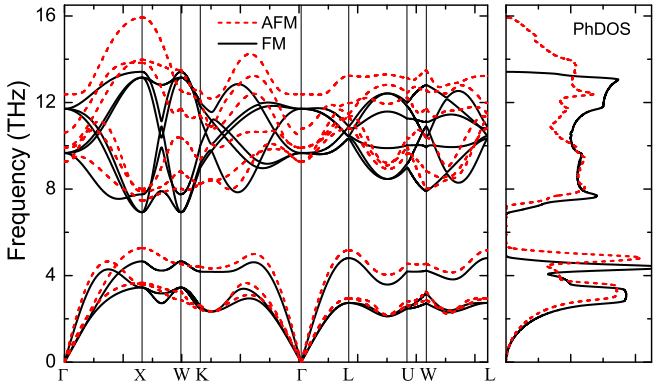

FIG. 9: (Color online) Phonon dispersion curves (left panel) and corresponding PhDOS (right panel) for the AFM and FM states calculated with LDA+U using U=4 eV.

along Γ–X–W–K–Γ–L–U–W–L directions in the BZ as well as the PhDOS, which are displayed in Fig. 9 for FM and AFM states with LDA+U (U=4 eV). To our knowledge, there are no experimental and theoretical phonon results available in literature for CmO_2. Our previously reported phonon curves and/or PhDOS for PuO_2 [19] and UO_2 [20] have been examined recently by experiments [9, 12, 21] showing good agreements. So, our present phonon results for CmO_2 here may find their instructive significance for experiments and theoretical calculations in future. Besides, the Born effective charges, responsible for the longitudinal optical (LO)-transverse optical (TO) splitting near the Γ point in BZ, of Cm and O ions for FM (AFM) state are calculated to be $Z^*_{\rm Cm}$ = 1.07 (4.41) and $Z^*_{\rm O}$ = −0.46 (−2.19), respectively. The values for AFM state are comparable with NpO_2, PuO_2, UO_2, and AmO_2 [17, 19, 20, 26].

In the primitive cell of the fluorite CmO_2, there are only three atoms (one Cm and two O atoms). So, there are nine phonon modes in the phonon dispersion. We can see that there appears a phonon gap between the optic modes and the acoustic branches of about 2.1 (2.0) THz for FM (AFM) state. This kind of phonon gap has never been found in other AO_2 for A=Th to Am [17, 19, 20, 25, 26]. Because curium atoms are heavier than these actinides, the appearance of the phonon gap is understandable. The phonon frequencies of AFM state are larger than that of FM state, especially for the two LO modes. This is due to the fact that the lattice constants of AFM state are smaller than that of FM state. Since the amplitudes of the Born effective charges of AFM state are dramatically larger than that of FM state, the LO-TO splitting in AFM state is evident while in FM state is almost invisible. Besides, the PhDOS of FM (AFM) can be viewed as two parts. One part is lower than 4.8 (5.3) THz with the main contribution from curium sublattice while the other part is higher than 6.9 (7.3) THz with the main contribution from oxygen sublattice.

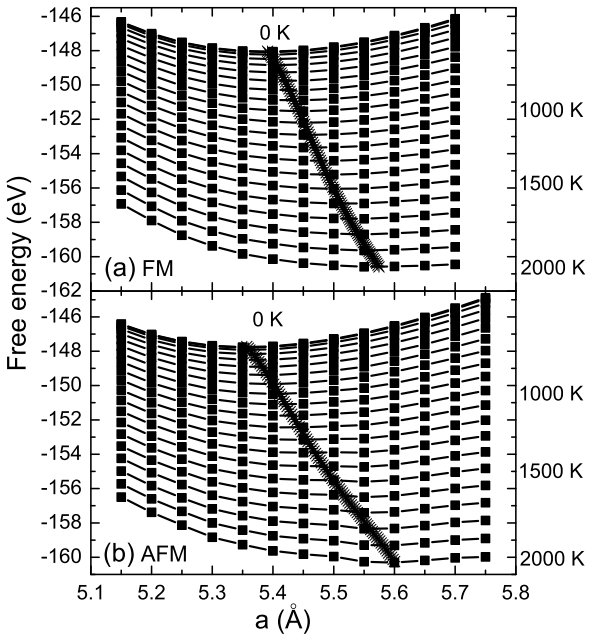

FIG. 10: (Color online) Dependences of the free energy $F(T,V)$ on the lattice parameter a at various temperatures for (a) FM and (b) AFM states calculated with LDA+U using U=4 eV.

E. Thermodynamic properties

Using U=4 eV within LDA+U, the free energy curves $F(T,V)$ for temperatures ranging from 0 up to 2000 K for FM and AFM states are calculated (see Fig. 10). Within QHA [51], the ground-state total energy $E(V)$ and the phonon free energy $F_{ph}(T,V)$ are calculated by constructing several 2×2×2 supercells. From our calculated $F(T,V)$ at several constant temperatures, without or with considering of the thermal electronic contribution $F_{el}(T,V)$, the equilibrium lattice parameter $a(T)$ and bulk modulus $B(T)$ are obtained by EOS fitting and are presented in Fig. 11. The thermal-expansion coefficients $\alpha_V(T)$ are presented in Fig. 12 together with the experimental results [74, 75] and other theoretical results [31]. The $a(T)$ with contribution of the F_{el} are also showed in Fig. 10.

As shown in Fig. 11(a), the lattice parameters $a(T)$ for both magnetic states increase steadily upon increasing temperature. This kind of expansion has also been observed in our previous study of PuO_2 [19] and UO_2 [20]. The effect of the thermal electronic contribution for AFM state is very strong while that for FM state is weak. This is because the values of $D(\epsilon_F)$ for FM state are almost constant upon changing volumes while that for AFM state increase dramatically with increasing volumes. Increasing temperature over about 1500 K, the $a(T)$ values for AFM state are turned to larger than that for FM state. Our calculated values of $\alpha_V(T)$ are larger than the experimental results [74, 75] but the

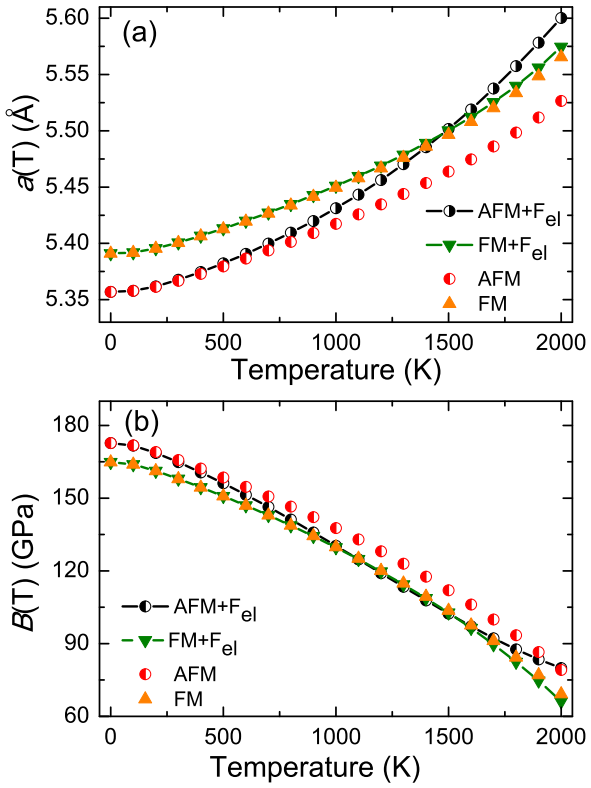

FIG. 11: (Color online) Temperature dependences of (a) lattice parameter $a(T)$ and (b) bulk modulus $B(T)$ for FM and AFM states with and without the electronic contribution.

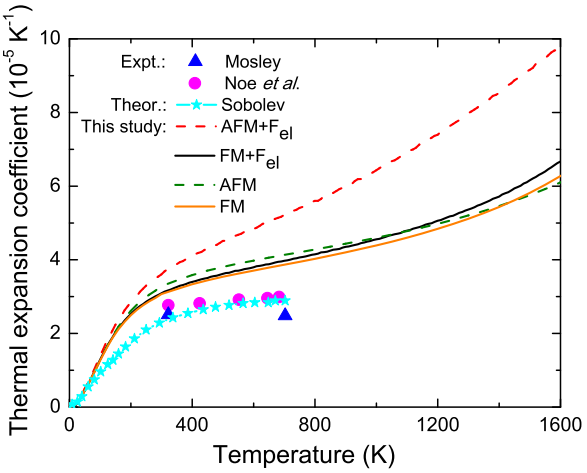

FIG. 12: (Color online) Temperature dependences of thermal expansion coefficients for FM and AFM states with and without the electronic contribution. Experimental results from Refs. [74, 75] and other theoretical results from Ref. [31] are also show for comparison.

TABLE V: The average mode Grüneisen parameters $\bar{\gamma}_j$ and group velocities υ_j ($\times 10^2$ m/s) of FM and AFM states along the [001], [011] and [111] crystal directions. Since that the symmetry along the [001] and [111] directions is high, the two transverse vibration branches are degeneracy, thus, they are presented as one value.

Branch	FM					
	$\bar{\gamma}_j$			υ_j		
	[001]	[011]	[111]	[001]	[011]	[111]
TA	0.99	1.10/1.30	0.88	5.13	3.40/4.11	3.16
LA	1.92	2.01	2.10	6.97	4.46	5.53
TO	1.74	2.31/1.84	2.15	-3.89	-2.05/-1.57	0.92
LO	1.70	1.93	2.12	-2.68	-1.29	1.09
TO′	1.08	1.13/1.14	0.86	2.34	0.90/0.98	-1.24
LO′	0.90	1.00	0.94	2.79	1.81	-0.75
	AFM					
TA	1.70	1.69/2.06	1.49	5.34	3.56/4.38	3.32
LA	2.74	2.53	2.54	7.79	4.97	5.90
TO	1.46	1.35/0.98	0.94	-1.79	-1.17/-0.58	1.09
LO	1.55	1.87	1.33	-2.10	0.63	2.76
TO′	1.74	2.11/2.06	2.08	5.87	3.43/3.94	1.59
LO′	2.49	2.50	3.01	8.96	5.70	3.84

trends agree.

For bulk modulus $B(T)$, evident decreasing behaviors are found with increasing temperature for both FM and AFM states. The effect of the thermal electronic contribution here is very weak. Specifically, the amplitude of such a change between 0 and 1500 K for AFM state of CmO_2 is ∼70.3 GPa, which is larger than that of UO_2 [20] and PuO_2 [19] by about 43.5 and 49.7 GPa, respectively. This fact indicates that CmO_2 will be softened quicker upon increasing temperature in comparison with UO_2 and PuO_2.

The calculated specific heat at constant volume C_V, specific heat at constant pressure C_P and entropy S are shown in Fig. 13. In calculating of the C_P, the thermal electronic contribution has been included. It can be seen that the C_V increases quickly up to room temperature and becomes close to a constant in the Dulong-Petit limit [76]. Over the Debye temperature, the C_P increases continuously. In temperature range of 300-650 K, our calculated values of C_P agree well with experiment [28] and other theoretical results [31, 77]. We never find evident differences between the FM and AFM states for $T < 900$ K, over which the differences become larger and lager with increasing temperature. This kind of temperature effect originates from aforementioned difference of the thermal electronic contributions between these two magnetic states. The temperature-dependent behaviors of the S are similar with that of other AO_2, such as UO_2 [20]. Over 50 K, the S of CmO_2 becomes to be slightly larger than that of UO_2. The electronic contribution to the S is very small, in a magnitude of about 10^{-2}, when comparing with the lattice contribution. The differences between the FM and AFM states are limited.

In order to discuss the anharmonic effects in CmO_2,

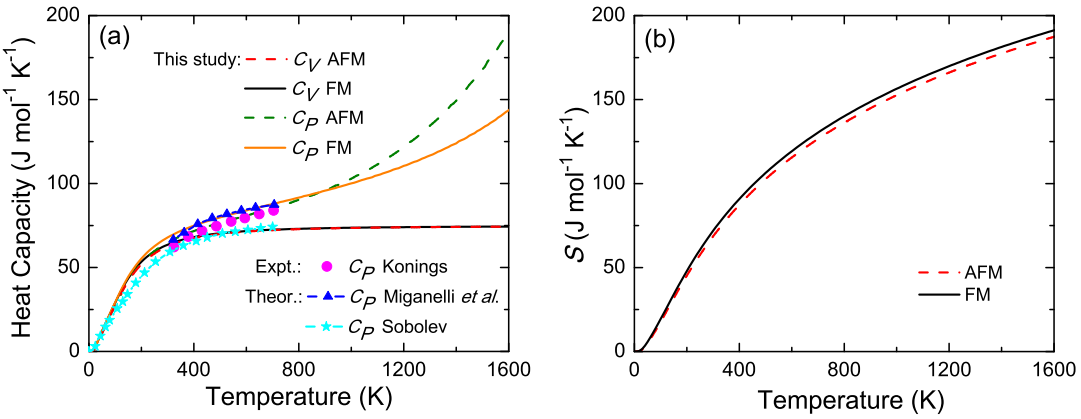

FIG. 13: (Color online) Temperature dependences of (a) specific heat at constant volume (C_V) and constant pressure (C_P) as well as (b) entropy for FM and AFM states. Experimental [28] and other theoretical [31, 77] results of C_P are presented.

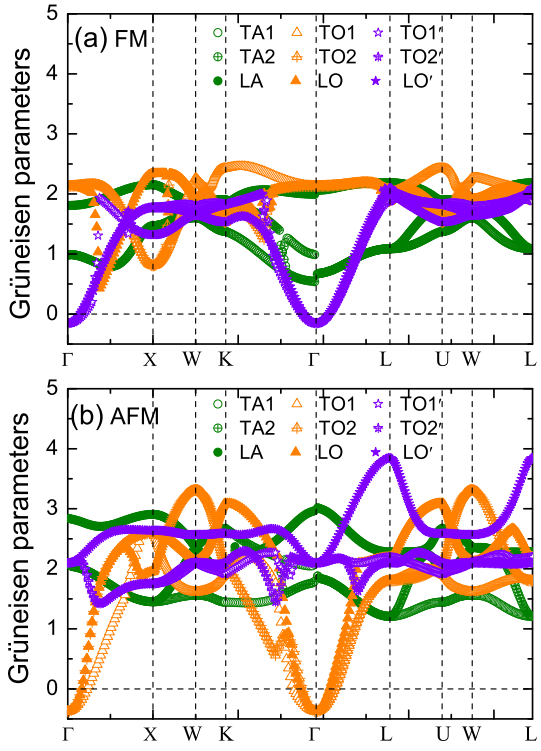

FIG. 14: (Color online) Theoretically calculated Grüneisen dispersions along high-symmetry directions in the reciprocal lattice space for (a) FM and (b) AFM states. The acoustic branches, circles; the first optical branches, triangles; the second optical branches, pentagrams.

we calculate the Grüneisen parameters for each vibration mode $\gamma_j(\mathbf{q})$ according to Eq. (11) by expanding and compressing the equilibrium volume ∼1%. Based upon our calculated phonon spectra, we plot the mode Grüneisen parameters along $\Gamma{-}X{-}W{-}K{-}\Gamma{-}L{-}U{-}W{-}L$ directions in Figs. 14(a) and 14(b) for FM and AFM states, respectively.

For FM state, we find that the second optical branches (TO1′, TO2′ and LO′) of the Grüneisen parameters have some negative values near the Γ point. All other branches are positive in the whole BZ. At U point, the largest value of the mode Grüneisen parameter appears on the first transverse optical branches (TO1), close to 2.4. All the branches distribute mainly in range from 0.5 to about 2.4. As for AFM state, the first optical branches (TO1 TO2 and LO) have some negative values near the Γ point. The largest value of about 3.8 appears at L point for the LO′ mode. The main distribution of $\gamma_j(\mathbf{q})$ is in range from 1.2 to 3.3. This fact indicates that the anharmonic effect in AFM state is stronger than that in FM state.

To quantitatively analyze the anharmonic effects along typical crystalline directions, we calculate the average mode Grüneisen parameters $\bar{\gamma}_j$ along the $\Gamma - X$, $\Gamma - K$ and $\Gamma - L$ directions through $\bar{\gamma}_j = \sum \gamma_j(\mathbf{q}) / \sum(\mathbf{q})$ and present them in Table V. The $\Gamma - X$, $\Gamma - K$ and $\Gamma - L$ in BZ stand for the [001], [110] and [111] orientations of the CmO_2 unit cell, respectively. As indicated in Table V, the largest average value for FM state appear on the TO1 branch along the [011] direction while for AFM state is on the LO′ branch along the [111] direction. These results illustrate large anharmonicity of the TO1 mode for FM and the LO′ mode for AFM state. From Table V, we can summarize the Grüneisen parameters values on nine branches and along the three typical crystalline directions. We obtain $\bar{\gamma}(CmO_2)$=38.84/49.63 for FM/AFM state. The result of AFM CmO_2 is slightly larger than that of AFM UO_2 [$\bar{\gamma}(UO_2)$=46.06] but smaller than that of AFM PuO_2 [$\bar{\gamma}(PuO_2)$=61.86] [78]. Thus, we can say that the anharmonic effect of CmO_2 is comparable with UO_2 but is weaker than that of PuO_2. Understanding of the anharmonic effect is critical for our following study of the thermal conductivity.

The thermal conductivity of actinides plays important role in nuclear industries. To study the lattice thermal conductivity, we firstly analyze the phonon group ve-

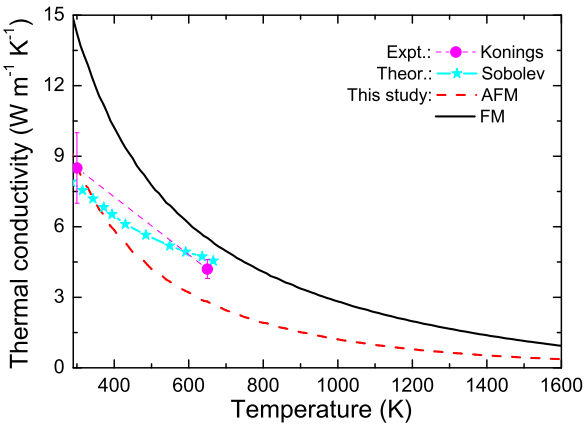

FIG. 15: (Color online) Theoretically calculated lattice thermal conductivity for FM and AFM states, together with available experimental [28] and other theoretical [31] results.

locities υ_j, $\upsilon_j=\frac{d\omega_j(\mathbf{q})}{d\mathbf{q}}$, since their tight relationship of $\kappa_L \propto \upsilon_j$. We deduce the phonon group velocities υ_j of FM and AFM states along the [001], [011] and [111] crystalline directions by utilizing the phonon spectra data $\omega_j(\mathbf{q})$ in Fig. 9 and present them in Table V. As seen in Table V, only the TA and LA branches of FM state exhibit larger phonon group velocities than other branches while for AFM state the TA, LA, TO′, and LO′ branches show relatively large phonon group velocities, especially along the [001] direction. These phonon modes should be regarded as good heat carriers. However, the large anharmonic effect may constrain the heat-transfer ability at high temperature, such as the LO′ mode for AFM state.

After summarizing, we obtain the total phonon group velocities of FM (AFM) CmO_2 along the [001], [011], and [111] directions to be 35.16 (44.85) $\times$ 10^2, 20.57 (28.36) $\times$ 10^2, and 18.01 (24.50) $\times$ 10^2 m/s, respectively. These data clearly indicate that the AFM CmO_2 shows larger phonon group velocities than FM CmO_2. The result of AFM CmO_2 is slightly larger than that of AFM UO_2 (39.42 $\times$ 10^2, 26.60 $\times$ 10^2, and 20.90 $\times$ 10^2 m/s, respectively) but smaller than that of AFM PuO_2 (62.87 $\times$ 10^2, 39.6 $\times$ 10^2, and 25.73 $\times$ 10^2 m/s, respectively) [78].

After aforementioned analysis, one can believe that the acoustic branches of the two magnetic states play critical role in heat transfer no matter at low temperature or at high temperature. However, the optical modes may only contribute mainly to the heat transfer at low temperature. Their contribution at high temperature is limited by the anharmonic-induced shorter mean free path. After ignoring the contribution from optical branches, we calculate the thermal conductivity for FM and AFM states in temperature range of 300−1600 K by the Slack relation and plot them in Fig. 15.

At 300 K, our calculated k_L for AFM/FM state is 8.6/14.2 $Wm^{-1}K^{-1}$. The value of the AFM CmO_2 is in good agreement with experiment value of 7-10 $Wm^{-1}K^{-1}$ at 298.15 K [28]. The value of the FM state is very large. This is because our calculated values of the Grüneisen parameters for FM state are smaller than that for AFM state. At room temperature, the actual experimental sample of CmO_2 may be the paramagnetic state. Thus, the AFM model is more suitable than the FM model. Increasing temperature to 650 K, the experimental value of 3.8-4.6 $Wm^{-1}K^{-1}$ [28] is well in between our calculated k_L for AFM (2.8 $Wm^{-1}K^{-1}$) and FM (5.5 $Wm^{-1}K^{-1}$) states. From 300 to 650 K, most values of the theoretical results [31] are also in between our results for AFM and FM. Comparing with other AO_2 [78, 79], the thermal conductivity of AFM CmO_2 in temperature range of 300-650 K decreases more rapidly than that of ThO_2 and PuO_2, comparable to UO_2. Above 650 K, same with other AO_2, the decrease behavior of k_L is slow down.

IV. DISCUSSION

CmO_2 is a member of actinides and has rich physics to explore. However, there are very limited reports having investigated this important $5f$ strong correlated system. Our first-principles simulations here give a detail analysis on the strong Coulomb repulsion and the SOC effects for CmO_2. Without including the Coulomb repulsion, using pure LDA or GGA, a localized distribution of the $5f$ orbital above the O-$2p$ orbital is observed and a metallic state is predicted for all considered magnetic states. After including the Coulomb repulsion, both LDA+U and GGA+U still result in a metallic state but with localized $5f$ orbital becoming below the O-$2p$ orbital. Only using LDA+U+SOC can one obtain the charge-transfer semiconductor state for AFM configuration, consistent with previous HSE [5, 62] and SIC-LSD [6] results. Through carefully comparing, the FM state with half-metallic character is predicted to be energetically stable. This fact is different with many other AO_2, of which the AFM state is predicted to be more stable. For both AFM and FM states, our calculated elastic constants and phonon spectra indicate that they are mechanically and dynamically stable. Compare with experiments [27, 29, 30], our LDA+U(+SOC) calculations can predict reasonable results of lattice parameters and magnetic moments. In comparing with other AO_2, we present reasonable results of the lattice parameters, magnetic states, electronic density of states, band gaps, and elastic constants. We find that including both Coulomb repulsion and SOC is necessary in study of global minimum magnetic states and reasonable electronic structures for many AO_2. In study of the macroscopic properties like elasticity and thermodynamics, the SOC can be neglected [20, 71].

Using LDA+U, we present phonon spectra and various thermodynamic data for CmO_2, as it being a member of nuclear material. Most of these data are firstly reported,

such as the phonon spectra, Gibbs free energy, Grüneisen parameters, and phonon group velocities. Our results indicate that the DFT at the level of LDA+U approach works well to simulate these thermodynamic properties and can be easily extend to other systems, like U_3O_8 and U_2O_5.

V. CONCLUSION

In summary, the ground-state properties of CmO_2 are explored with first-principles LDA/GGA+U approaches. We calculate the equilibrium lattice parameters, bulk modulus, and one-electron behaviors of $5f$ state with diverse values of Coulomb repulsion parameter U. By choosing the Hubbard U parameter around 4 eV within the LDA+U approach, the calculated lattice parameters for FM and AFM states are in good agreement with experiments. For energetically-stable FM state, we only predict metallic state no matter increasing U to 6 eV or inclusion SOC in our calculations. The main electronic occupation near the Fermi level is turned over by the strong Coulomb repulsion from U-$5f$ to O-$2p$. Same with our previous reports of other AO_2 [17, 19, 20, 25, 26], the Cm-O bonds in CmO_2 also can be interpreted as displaying a mixed ionic/covalent character. The stability of the two magnetic phases is predicted through calculating elastic constants and phonon dispersion. Among AO_2, a phonon gap of $\sim$2 THz is firstly reported for CmO_2 and need further experiments to verify. Based on our calculated E-V data, phonon spectra, and electronic density of state at the Fermi level, we obtain the Gibbs free energy, thermal expansion coefficient, specific heat, entropy, Grüneisen parameters, phonon group velocities, and lattice thermal conductivity. The effect of the thermal electronic contribution on some of these properties for AFM state is very strong while that for FM state is weak. In temperature range of 300-650 K, our calculated values of C_P agree well with experiment [28]. The anharmonic effect of AFM CmO_2 is comparable with UO_2 but is weaker than that of PuO_2 [78]. Our calculated k_L at 300 K for AFM state is in good agreement with experiment [28].

Acknowledgments

B.T.W. thanks Weiwei Sun at Oak Ridge National Laboratory for fruitful discussions. W.D.L. and F.W. acknowledge financial support from National Natural Science Foundation of China under Grant Nos. 51371195, 11675255, 11374197, and 11634008. O.E. acknowledges financial support from KAW (Projects No. 2013.0020 and No. 2012.0031). The calculations were performed at Supercomputer Centre in China Spallation Neutron Source.

[1] S. Heathman, R. G. Haire, T. Le Bihan, A. Lindbaum, M. Idiri, P. Normile, S. Li, R. Ahuja, B. Johansson, and G. H. Lander, Science **309**, 110 (2005).
[2] R. Atta-Fynn and A. K. Ray, Phys. Rev. B **76**, 115101 (2007).
[3] K. T. Moore and G. van der Laan, Rev. Mod. Phys. **81**, 235 (2009).
[4] I. D. Prodan, G. E. Scuseria, and R. L. Martin, Phys. Rev. B **73**, 045104 (2006).
[5] I. D. Prodan, G. E. Scuseria, and R. L. Martin, Phys. Rev. B **76**, 033101 (2007).
[6] L. Petit, A. Svane, Z. Szotek, W. M. Temmerman, and G. M. Stocks, Phys. Rev. B **81**, 045108 (2010).
[7] Q. Yin, A. Kutepov, K. Haule, G. Kotliar, S. Y. Savrasov, and W. E. Pickett, Phys. Rev. B **84**, 195111 (2011).
[8] X. D. Wen, R. L. Martin, G. E. Scuseria, S. P. Rudin, and E. R. Batista, J. Phys. Chem. C **117**, 13122 (2013).
[9] J. W. L. Pang, W. J. L. Buyers, A. Chernatynskiy, M. D. Lumsden, B. C. Larson, and S. R. Phillpot, Phys. Rev. Lett. **110**, 157401 (2013).
[10] T. Bo, J. H. Lan, Y. L. Zhao, Y. J. Zhang, C. H. He, Z. F. Chai, and W. Q. Shi, J. Nucl. Mater. **454**, 446 (2014).
[11] T. Bo, J. H. Lan, C. Z. Wang, Y. L. Zhao, C. H. He, Y. J. Zhang, Z. F. Chai, and W. Q. Shi, J. Phys. Chem. C **118**, 21935 (2014).
[12] J. W. L. Pang, A. Chernatynskiy, B. C. Larson, W. J. L. Buyers, D. L. Abernathy, K. J. McClellan, and S. R. Phillpot, Phys. Rev. B **89**, 115132 (2014).
[13] P. Seth, P. Hansmann, A. van Roekeghem, L. Vaugier, and S. Biermann, Phys. Rev. Lett. **119**, 056401 (2017).
[14] N. Lanatà, Y. X. Yao, X. Y. Deng, V. Dobrosavljević, and G. Kotliar, Phys. Rev. Lett. **118**, 126401 (2017).
[15] P. Maldonado, L. Paolasini, P. M. Oppeneer, T. R. Forrest, A. Prodi, N. Magnani, A. Bosak, G. H. Lander, and R. Caciuffo, Phys. Rev. B **93**, 144301 (2016).
[16] C. E. Boettger and A. K. Ray, Int. J. Quantum Chem. **90**, 1470 (2002).
[17] B. T. Wang, H. L. Shi, W. D. Li, and P. Zhang, Phys. Rev. B **81**, 045119 (2010).
[18] S. L. Dudarev, G. A. Botton, S. Y. Savrasov, C. J. Humphreys, and A. P. Sutton, Phys. Rev. B **57**, 1505 (1998).
[19] P. Zhang, B. T. Wang, and X. G. Zhao, Phys. Rev. B **82**, 144110 (2010).
[20] B. T. Wang, P. Zhang, R. Lizárraga, I. Di Marco, and O. Eriksson, Phys. Rev. B **88**, 104107 (2013).
[21] M. E. Manley, J. R. Jeffries, A. H. Said, C. A. Marianetti, H. Cynn, B. M. Leu, and M. A. Wall, Phys. Rev. B **85**, 132301 (2012).
[22] J. J. Zheng, B. T. Wang, I. Di Marco, and W. D. Li, Int. J. Hydrogen Energy **39**, 13255 (2014).
[23] M. Colarieti-Tosti, O. Eriksson, L. Nordstrom, J. M. Wills, and M. S. S. Brooks, Phys. Rev. B **65**, 195102 (2002).
[24] F. Zhou and V. Ozolins, Phys. Rev. B **83**, 085106 (2011).
[25] B. T. Wang, H. L. Shi, W. D. Li, and P. Zhang, J. Nucl. Mater. **399**, 181 (2010).
[26] Y. Lu, Y. Yang, F. W. Zheng, B. T. Wang, and P. Zhang,

J. Nucl. Mater. **441**, 411 (2013).
[27] J. P. Dancausse, R. G. Haire, S. Heathman, and U. Benedict, J. Nucl. Sci. Technol. **3**, 136 (2002).
[28] R. J. M. Konings, J. Nucl. Mater. **298**, 255 (2001).
[29] P. Villars and L. D. Calvert, Pearsons Handbook of Cystallographic Data for Intermetallic Phases, 2nd ed. (ASM International, Ohio, 1991).
[30] L. R. Morss, J. W. Richardson, C. W. Williams, G. H. Lander, A. C. Lawson, N. M. Edelstein, and G. V. Shalimoff, J. Less-Common Met. **156**, 273 (1989).
[31] V. Sobolev, J. Nucl. Mater. **389**, 45 (2009).
[32] S. Li, R. Ahuja, and B. Johansson, High Press. Res. **22**, 471 (2002).
[33] F. Niikura and T. Hotta, Phys. Rev. B **83**, 172402 (2011).
[34] J. T. Pegg, X. Aparicio-Anglès, M. Storr, and N. H. de Leeuw, J. Nucl. Mater. **492**, 269 (2017).
[35] M. T. Suzuki, N. Magnani, and P. M. Oppeneer, Phys. Rev. B **88**, 195146 (2013).
[36] V. Milman, B. Winkler, and C. J. Pickard, J. Nucl. Mater. **322**, 165 (2003).
[37] A. Bouasria, A. Zaoui, S. Ait Abderrahmane, S. Kacimi, A. Boukortt, M. Bejar, and E. Dhahri, Int. J. Comput. Mater. Sci. Eng. **6**, 1750006 (2017).
[38] G. Kresse and J. Furthmüller, Phys. Rev. B **54**, 11169 (1996).
[39] W. Kohn and L. J. Sham, Phys. Rev. **140**, A1133 (1965).
[40] J. P. Perdew, K. Burke, and Y. Wang, Phys. Rev. B **54**, 16533 (1996).
[41] H. J. Monkhorst and J. D. Pack, Phys. Rev. B **13**, 5188 (1976).
[42] S. L. Dudarev, M. R. Castell, G. A. Botton, S. Y. Savrasov, C. Muggelberg, G. A. D. Briggs, A. P. Sutton, and D. T. Goddard, Micron **31**, 363 (2000).
[43] S. L. Dudarev, D. N. Manh, and A. P. Sutton, Philos. Mag. B **75**, 613 (1997).
[44] A. I. Liechtenstein, V. I. Anisimov, and J. Zaanen, Phys. Rev. B **52**, R5467 (1995).
[45] O. Eriksson, A. Bergman, L. Bergqvist, and J. Hellsvik, *Atomistic Spin Dynamics: Foundations and Applications* (Oxford University Press, Oxford, UK, 2017).
[46] F. Birch, Phys. Rev. **71**, 809 (1947).
[47] B. T. Wang, P. Zhang, H. Z. Song, H. L. Shi, D. F. Li, and W. D. Li, J. Nucl. Mater. **401**, 124 (2010).
[48] R. Hill, Phys. Phys. Soc. London **65**, 349 (1952).
[49] C. Cozzo, D. Staicu, J. Somers, A. Fernandez, and R. J. M. Konings, J. Nucl. Mater. **416**, 135 (2011).
[50] Y. Wang, L. Q. Chen, and Z. K. Liu, Comput. Phys. Commun. **185**, 2950 (2014).
[51] A. Siegel, K. Parlinski, and U. D.Wdowik, Phys. Rev. B **74**, 104116 (2006).
[52] P. Souvatzis, A. Delin, and O. Eriksson, Phys. Rev. B **73**, 054110 (2006).
[53] C. W. Greeff and M. J. Graf, Phys. Rev. B **69**, 054107 (2004).
[54] A. Sommerfeld and N. H. Frank, Rev. Mod. Phys. **3**, 1 (1931).
[55] Q. Yin, S.Y. Savrasov, Phys. Rev. Lett. **100** 225504 (2008).
[56] G. A. Slack, J. Phys. Chem. Solids **34**, 321 (1973)
[57] G. A. Slack, Solid State Phys. **34**, 1 (1979).
[58] M. A. Blanco, E. Francisco, and V. Luaña, Comput. Phys. Commun. **158**, 57 (2004).
[59] J. R. Peterson, J. Fuger, J. Inorg. Nucl. Chem. **33**, 4111 (1971) .
[60] B. C. Frazer, G. Shirane, D. E. Cox, and C. E. Olsen, Phys. Rev. **140**, A1448 (1965).
[61] A. Bendjedid, T. Seddik, R. Khenata, H. Baltache, G. Murtaza, A. Bouhemadou, S. Bin Omran, S. Azam, and S. A. Khan, J. Magn. Magn. Mater. **396**, 190 (2015).
[62] X. D. Wen, R. L. Martin, L. E. Roy, G. E. Scuseria, S. P. Rudin, E. R. Batista, T. M. McCleskey, B. L. Scott, E. Bauer, J. J. Joyce, and T. Durakiewicz, J. Chem. Phys. **137**, 154707 (2012).
[63] J. P. Dancausse, E. Gering, S. Heathman, and U. Benedict, High Press. Res. **2**, 381 (1990).
[64] M. Idiri, T. Le Bihan, S. Heathman, and J. Rebizant, Phys. Rev. B **70**, 014113 (2004).
[65] B. Dorado and P. Garcia, Phys. Rev. B **87**, 195139 (2013).
[66] Y. J. Zhang, B. T. Wang, Y. Lu, Y. Yang, P. Zhang, J. Nucl. Mater. **430**, 137 (2012).
[67] I. D. Prodan, G. E. Scuseria, J. A. Sordo, K. N. Kudin, and R. L. Martin, J. Chem. Phys. **123**, 014703 (2005).
[68] Y. Baer and J. Schoenes, Solid State Commun. **33**, 885 (1980).
[69] T. M. McCleskey, E. Bauer, Q. X. Jia, A. K. Burrell, B. L. Scott, S. D. Conradson, A. Mueller, L. Roy, X. D. Wen, G. E. Scuseria, and R. L. Martin, J. Appl. Phys. **113**, 013515 (2013).
[70] C. Suzuki, T. Nishi, M. Nakada, M. Akabori, M. Hirata, and Y. Kaji, J. Phys. Chem. Solids **73** 209 (2012).
[71] M. Sanati, R. C. Albers, T. Lookman, and A. Saxena, Phys. Rev. B **84**, 014116 (2011).
[72] J. F. Nye, Physical Properties of Crystals (Oxford University Press, Oxford, 1985).
[73] B. T. Wang, P. Zhang, H. L. Shi, B. Sun, and W. D. Li, Eur. Phys. J. B **74**, 303 (2010).
[74] M. Noé, J. R. Peterson, Inorg. Nucl. Chem. Let. **8**, 897 (1972).
[75] W. C. Mosley, J. Inorg. Nucl. Chem **34**, 539 (1972).
[76] C. Kittel, Introduction to Solid State Physics, 7th ed. (Wiley, New York, 1996).
[77] M. A. Mignanelli, R. Thetford, in *Workshop Proceedings Advanced Reactors with Innovative Fuels*, edited by British Nuclear Fuels Limited, (Chester, UK, 2001).
[78] B. T. Wang, J. J. Zheng, X. T. Qu, W. D. Li, and P. Zhang, J. Alloys Compd. **628**, 267 (2015).
[79] Y. Lu, Y. Yang, and P. Zhang, J. phys.: Condens. Matter. **24**, 225801 (2012).